# Chiral Spin Density Wave and $d+id$ Superconductivity in the Magic-Angle-Twisted Bilayer Graphene

Cheng-Cheng Liu,[1,†] Li-Da Zhang,[1,†] Wei-Qiang Chen,[2] and Fan Yang[1,*]
[1]School of Physics, Beijing Institute of Technology, Beijing 100081, China
[2]Shenzhen Institute for Quantum Science and Engineering and Department of Physics, Southern University of Science and Technology, Shenzhen 518055, China

(Received 26 April 2018; published 21 November 2018)

We model the newly synthesized magic-angle-twisted bilayer graphene superconductor with two $p_{x,y}$-like Wannier orbitals on the superstructure honeycomb lattice, where the hopping integrals are constructed via the Slater-Koster formulism by symmetry analysis. The characteristics exhibited in this simple model are well consistent with both the rigorous calculations and experiment observations. A van Hove singularity and Fermi-surface (FS) nesting are found in the doping levels relevant to the correlated insulator and unconventional superconductivity revealed experimentally, based on which we identify the two phases as weak-coupling FS instabilities. Then, with repulsive Hubbard interactions turned on, we performed random-phase-approximation based calculations to identify the electron instabilities. As a result, we find chiral $d+id$ topological superconductivity bordering the correlated insulating state near half-filling, identified as noncoplanar chiral spin-density wave ordered state, featuring the quantum anomalous Hall effect. The phase diagram obtained in our approach is qualitatively consistent with experiments.

DOI: 10.1103/PhysRevLett.121.217001

*Introduction.*—The newly revealed "high-temperature superconductivity (SC)" [1] in the "magic-angle" twisted bilayer-graphene (MA-TBG) has attracted great research interest [2–9]. In such a system, the low energy electronic structure can be dramatically changed by the twist. It was shown that some low energy flat bands, which are well separated with other high energy bands, appear when the twist angle is around 1.1°. A correlated insulating state is observed when the flat bands are near half-filled [10]. Doping this correlated insulator leads to SC with the highest critical temperature $T_c$ up to 1.7 K. This system looks similar to the cuprates in terms of the phase diagram and the high ratio of $T_c$ over the Fermi temperature $T_F$. In fact, it was argued that the insulating state was a Mott insulator, while the MA-TBG was an analogy of a cuprate superconductor. Since the structure of the MA-TBG is *in situ* tunable, it was proposed that this system can serve as a good platform to study the pairing mechanism of the high-$T_c$ SC, the biggest challenge of condensed-matter physics.

However, the viewpoint that the SC in MA-TBG is induced by doping a Mott-insulator suffers from the following three inconsistencies with experimental results. First, the so-called "Mott gap" extrapolated from the temperature-dependent conductance is just about 0.31 meV [10], which is much lower than the band width of the low energy emergent flat bands (∼10 meV). Such a tiny Mott gap can hardly be consistent with the "Mott-physics." Second, the behaviors upon doping into this insulating phase is different from those for doping a Mott insulator, as analyzed in the following for the positive filling as an example. In the case of electron doping with respect to the half-filling, the system has a small Fermi pocket with an area proportional to doping, which is consistent with a doped Mott insulator [1]. However, in the hole doping case, slightly doping leads to a large Fermi surface (FS) with an area proportional to the electron concentration of the whole band, instead of the hole concentration with respect to the half-filling [1,10]. Such behavior obviously conflicts with the Mott physics. Third, some samples which exhibit the so-called "Mott-insulating" behavior at high temperature become SC upon lowering the temperature [11]. Such behavior is more like to be caused by competing between SC and some other kind of order, such as density waves, instead of Mott physics.

In this Letter, we study the problem from the weak coupling approach, wherein electrons on the FS acquire effective attractions through exchanging spin fluctuations, which leads to Cooper pairing. After analyzing the characteristics of the low energy emergent band structure, an effective $p_{x,y}$-orbital tight-binding model [6] on the emergent honeycomb lattice is adopted, but with the hopping integrals newly constructed via the Slater-Koster formulism [12], which is rederived based on the symmetry of the system (Supplemental Material, Sec. I [13]). The characteristics of the constructed band structure are qualitatively consistent with both the rigorous multiband tight-binding results [16,17] and experiments [1,10]. Moreover, the band degeneracy at high-symmetric points or lines is compatible with the corresponding irreducible representations [6]. Then, after the Hubbard-Hund interaction turns on, we performed RPA based calculations to study the electron instabilities. Our

 

results identify the correlated insulator near half-filling as a FS-nesting induced noncoplanar chiral spin-density wave (SDW) insulator, featuring a quantum anomalous Hall effect (QAHE). Bordering this SDW insulator is a chiral $d+id$ topological superconducting state. The obtained phase diagram is qualitatively consistent with experiments.

*The model.*—For the MA-TBG, the small twist angle between the two graphene layers, causes a Moire pattern which results in a much enlarged unit cell, consequently thousands of energy bands are taken into account [16,17], and the low-energy physics are dramatically changed [16–38]. Remarkably, four low energy nearly flat bands with a total bandwidth of about 10 meV emerge which are well isolated from the high energy bands. Since both the correlated insulating and the superconducting phases emerge when these low energy bands are partially filled, providing an effective model with relevant degrees of freedom to capture the low energy band structure is urgent.

By analyzing the degeneracy and representation of the flat bands at all three of the high symmetry points $\Gamma$, $K$, and $M$, a honeycomb lattice rather than the triangular one should be adopted to model the low-energy physics of MA-TBG [4,6]. The emergent honeycomb lattice consists of two sublattices originating from different layers. Further symmetry analysis shows that the related Wannier orbitals on each site belong to the $p_x$ and $p_y$ symmetry [6]. Therefore, we can construct the hopping integrals between the $p_{x,y}$-like orbitals on the honeycomb lattice via the Slater-Koster formulism [12] based on symmetry analysis [13], which reflects coexisting $\sigma$ and $\pi$ bondings [39–43]. Our tight-binding (TB) model up to the next nearest neighbor (NNN) hopping, thus obtained, reads

$$H_{tb}=\sum_{i\mu,j\nu,\sigma}t_{i\mu,j\nu}c^{\dagger}_{i\mu\sigma}c_{j\nu\sigma}-\mu_c\sum_{i\mu\sigma}c^{\dagger}_{i\mu\sigma}c_{i\mu\sigma}. \quad (1)$$

Here, $\mu$, $\nu=x$, $y$ represents the $p_x$, $p_y$ orbitals shown in Fig. 1(a), $i$, $j$ stand for the site and $\mu_c$ is the chemical potential determined by the filling $\delta\equiv n/n_s-1$ relative to charge neutrality. Here, $n$ is the average electron number per unit cell, $n_s=4$ is the $n$ for charge neutrality. The hopping integral $t_{i\mu,j\nu}$ can be obtained as

$$t_{i\mu,j\nu}=t^{ij}_{\sigma}\cos\theta_{\mu,ij}\cos\theta_{\nu,ij}+t^{ij}_{\pi}\sin\theta_{\mu,ij}\sin\theta_{\nu,ij}, \quad (2)$$

where $\theta_{\mu,ij}$ denotes the angle from the direction of $\mu$ to that of $\mathbf{r}_j-\mathbf{r}_i$. The Slater-Koster parameters $t^{ij}_{\sigma/\pi}$ represent the hopping integrals contributed by $\sigma/\pi$ bondings. More details about the band structure are introduced in the Supplemental Material, Sec. II [13].

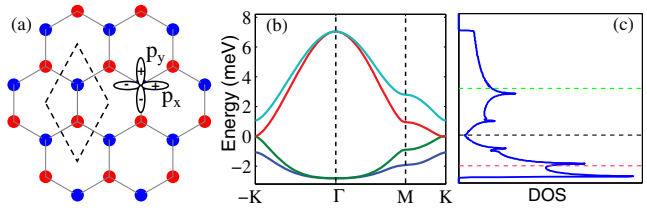


FIG. 1. (a) Schematic diagram for our model. The dashed rhombus labels the unit cell of the emergent honeycomb lattice with the $p_x$, $p_y$-like Wannier orbitals on each site. (b) Band structure and (c) DOS of MA-TBG. The red, black, and green horizontal dashed lines in (c) label the filling $\delta$ of $-\frac{1}{2}$, 0, and $\frac{1}{2}$, respectively. The Slater-Koster parameters $t^{ij}_{\sigma/\pi}$ are chosen as $t^{(1)}_{\sigma}=2$ meV, $t^{(1)}_{\pi}=t^{(1)}_{\sigma}/1.56$, $t^{(2)}_{\sigma}=t^{(1)}_{\sigma}/7$, and $t^{(2)}_{\pi}=t^{(2)}_{\sigma}/1.56$. Here, the superscript $(1)/(2)$ represents NN or NNN bondings, respectively.

The band structure of our TB model (1) is shown in Fig. 1(b). Investigating the degeneracy pattern here, one finds that the $\Gamma$ point is doubly degenerate for each of the two bands, the $M$ point is nondegenerate, and as for the two $K$ points, both degenerate Dirac crossing and nondegenerate splitting (Dirac mass generation) coexist. Such a degeneracy pattern is consistent with both symmetry representation [4,6] and rigorous results [16,17]. Note that the Dirac mass generation is important [6] in understanding the quantum oscillation experiment, wherein fourfold Landau level degeneracy (including spin degeneracy) is observed near the charge neutrality [1]. The model parameters $t^{ij}_{\sigma/\pi}$ [introduced in the caption of Fig. 1(a)] are tuned so that the renormalized Fermi velocity (which is about $\frac{1}{25}$ of that of monolayer graphene), as well as the total bandwidth (about 10 meV) are consistent with experiments. Note that, due to the presence of NNN hoppings, the band structure is particle-hole asymmetric with the negative ($n$) energy part flatter than the positive ($p$) part, consistent with experiment [1]. The density of states (DOS) shown in Fig. 1(c) suggests that the $\pm\frac{1}{2}$ fillings relevant to experiments are near the van Hove (VH) fillings $\delta_V$ ($\approx\pm0.425$) introduced below.

The evolution of the FS with filling near $\pm\frac{1}{2}$ is shown in Fig. 2. One finds that, in both the $n$ and $p$ parts, a Lifshitz transition takes place at some critical fillings $\delta_V$, which changes the FS topology. At the Lifshitz transition point, there is VH singularity (VHS) at the three $M$ points, and the FS is nearly perfectly nested, as shown in Figs. 2(b) and 2(e), with the three marked nesting vectors $\boldsymbol{Q}_\alpha$ ($\alpha=1, 2, 3$) also near the three $M$ points. One finds that the situation of FS nesting is asymmetric before and after the Lifshitz transition: before $\delta_V$, there are three FS patches with bad nesting; after $\delta_V$, two FS patches are left with the outer one well nested. This asymmetry on FS nesting is closely related to the asymmetry in the phase diagram studied below. Note that the $|\delta_V|$ for the $p$ and $n$ parts are only approximately equal. As shown in the Supplemental Material, Sec. II [13], these characteristics don't obviously change with model parameters in a reasonable range and $\delta_V$ is generally near $\pm\frac{1}{2}$.

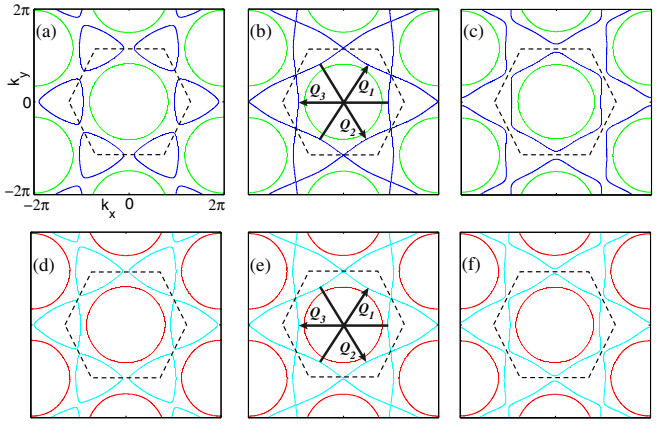


FIG. 2. The evolution of FS. (a)–(c) FS at fillings −0.40, −0.425 ($\delta_V$), and −0.45. (d)–(f) FS at fillings 0.41, 0.425 ($\delta_V$) and 0.44. The central hexagons in every plot outlined with black dashed lines indicate the Brillouin Zone. The FS-nesting vectors $\boldsymbol{Q}_\alpha$ ($\alpha = 1, 2, 3$) are marked in (b) and (e).

It is proposed, here, that the SC detected in the MA-TBG is driven, not by electron-phonon coupling, but by electron-electron interactions (See Supplemental Material, Sec. III [13] for the analysis). We adopt the following repulsive Hubbard-Hund model proposed in Ref [6]:

$$\begin{aligned} H &= H_{tb} + H_{\text{int}} \\ H_{\text{int}} &= U\sum_{i\mu} n_{i\mu\uparrow}n_{i\mu\downarrow} + V\sum_{i} n_{ix}n_{iy} + J_H\sum_{i} \\ &\quad\times\left[\sum_{\sigma\sigma'} c^\dagger_{ix\sigma}c^\dagger_{iy\sigma'}c_{ix\sigma'}c_{iy\sigma} + (c^\dagger_{ix\uparrow}c^\dagger_{ix\downarrow}c_{iy\downarrow}c_{iy\uparrow} + \text{H.c.})\right], \end{aligned} \tag{3}$$

where $U = V + 2J_H$. Adopting $U = 1.5$ meV, we have considered both $J_H = 0.1U$ and $J_H = 0$, with the two cases giving qualitatively the same results. Strictly speaking, the Hubbard-Hund interactions $H_{\text{int}}$ describing the atomic interactions do not apply here for our extended effective orbitals. However, as will be seen, the electron instabilities here are mainly determined by the VHS and the FS nesting, and will not be strongly affected by the concrete formulism of the interactions, as long as it is repulsive. Therefore, model (3) can be a good starting point.

*Electron instabilities and phase diagram.*—We adopt the standard multiorbital RPA approach [14,15,44,45] to study the electron instabilities of the system. We start from the normal-state susceptibilities in the particle-hole channel and consider its renormalization due to interactions up to the RPA level. Through exchanging spin or charge fluctuations represented by these susceptibilities, the electrons near the FS acquire effective attractions, which leads to pairing instability for arbitrarily weak interactions. However, when the repulsive interaction strength $U$ rises to some critical value $U_c$, the spin susceptibility diverges, which leads to SDW order. More details can be found in the Supplemental Material Sec. III [13].

The bare susceptibility tensor is defined as,

$$\begin{aligned} \chi^{(0)l_1l_2}_{l_3l_4}(\boldsymbol{k},\tau) \equiv \frac{1}{N}\sum_{\boldsymbol{k}_1\boldsymbol{k}_2}\langle T_\tau c^\dagger_{l_1}(\boldsymbol{k}_1,\tau)c_{l_2}(\boldsymbol{k}_1+\boldsymbol{k},\tau) \\ \times c^\dagger_{l_3}(\boldsymbol{k}_2+\boldsymbol{k},0)c_{l_4}(\boldsymbol{k}_2,0)\rangle_0. \end{aligned} \tag{4}$$

Here, $\langle\cdots\rangle_0$ denotes the thermal average for the non-interacting system, and $l_{i(i=1,\ldots,4)} = 1, 2, 3, 4$ are the sublattice-orbital indices. Fourier transformed to the imaginary frequency space, the obtained $\chi^{(0)l_1,l_2}_{l_3,l_4}(\boldsymbol{k}, i\omega_n)$ can be taken as a matrix with $l_1l_2/l_3l_4$ to be the row or column indices. The largest eigenvalue $\chi(\boldsymbol{k})$ of the zero-frequency susceptibility matrix $\chi^{(0)l_1l_2}_{l_3l_4}(\boldsymbol{k}, i\omega_n = 0)$ as a function of $\boldsymbol{k}$ for $\delta \to \delta_V = -0.425$ is shown in the whole Brillouin Zone in Fig. 3(a), and along the high-symmetry lines in Fig. 3(b).

Figures 3(a) and 3(b) show that the distribution of $\chi(\boldsymbol{k})$ for $\delta \to \delta_V$ peaks near the three $M$ points in the Brillouin zone, which originates from the FS nesting shown in Fig. 2(b). In the thermal-dynamic limit, these peaks will diverge due to diverging DOS. Therefore, arbitrarily weak interactions will induce a density-wave type of instability. The RPA treatment shows that repulsive interactions suppress the charge susceptibility $\chi^{(c)}$ and enhance the spin susceptibility $\chi^{(s)}$ (Supplemental Material, Sec. III [13]). Therefore, SDW order emerges for arbitrarily weak Hubbard interactions in our model at $\delta_V$. We identify the correlated insulator observed by experiment [10] to be the SDW insulator proposed here at $\delta_V$, which is near $\pm\frac{1}{2}$.

Note that the competition among the threefold degenerate FS-nesting vectors $\boldsymbol{Q}_\alpha$ ($\alpha = 1, 2, 3$) will drive non-coplanar SDW order with spin chirality, featuring a QAHE [46–49]. To clarify this point, let us extrapolate the eigenvectors $\xi(\boldsymbol{Q}_\alpha)$ corresponding to the largest eigenvalue of the susceptibility matrix $\chi^{(0)}(\boldsymbol{k}, i\omega_n = 0)$ for $\boldsymbol{k} \to \boldsymbol{Q}_\alpha$. Defining the magnetic order parameters $\boldsymbol{S}_{i\mu\nu} \equiv \langle c^\dagger_{i\mu s}\boldsymbol{\sigma}_{ss'}c_{i\nu s'}\rangle$, the divergence of $\chi(\boldsymbol{Q}_\alpha)$ requires spontaneous generation of magnetic order with $\boldsymbol{S}_{i\mu\nu} \propto \xi_{\mu\nu}(\boldsymbol{Q}_\alpha)e^{i\boldsymbol{Q}_\alpha\cdot\boldsymbol{R}_i}\boldsymbol{n}_\alpha$, with the global unit vector $\boldsymbol{n}_\alpha$ pointing anywhere. Now, we have three degenerate $\boldsymbol{Q}_\alpha$, which perfectly fit into the three

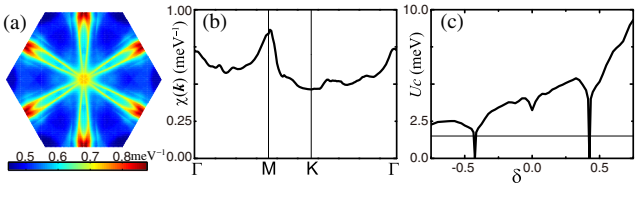


FIG. 3. Distribution of $\chi(\boldsymbol{k})$ for $\delta \to \delta_V = -0.425$ (a) in the Brillouin Zone, and (b) along the high-symmetric lines. (c) The filling dependence of $U_c$ (for $J_H = 0.1U$), with the horizontal line representing $U = 1.5$ meV adopted in our calculations.

spatial dimensions: $\boldsymbol{S}_{i\mu\nu} \propto [\xi_{\mu\nu}(\boldsymbol{Q_1})e^{i\boldsymbol{Q}_1\cdot\boldsymbol{R}_i}, \xi_{\mu\nu}(\boldsymbol{Q_2})e^{i\boldsymbol{Q}_2\cdot\boldsymbol{R}_i}, \xi_{\mu\nu}(\boldsymbol{Q_3})e^{i\boldsymbol{Q}_3\cdot\boldsymbol{R}_i}]$. Such noncoplanar SDW order with spin chirality may lead to a nontrivial topological Chern number in the band structure, resulting in a QAHE [46–49].

When the filling is away from $\delta_V$, SDW order only turns on when $U > U_c$, where the renormalized spin susceptibility tensor $\chi^{(s)}$ diverges. The filling dependence of $U_c$ for $J_H = 0.1U$ is shown in Fig. 3(c) (the case of $J_H = 0$ yields similar results), where SDW order is only present within a narrow regime centering at the two $\delta_V$. When $U < U_c$, through exchanging short-ranged spin and charge fluctuations between a Cooper pair, an effective pairing interaction vertex $V^{\alpha\beta}(\boldsymbol{k},\boldsymbol{k}')$ will be developed, which leads to the following linearized gap equation near $T_c$ (See Supplemental Material, Sec. III [13]):

$$-\frac{1}{(2\pi)^2}\sum_{\beta}\oint_{FS} dk'_{\parallel}\frac{V^{\alpha\beta}(\boldsymbol{k},\boldsymbol{k}')}{v_F^{\beta}(\boldsymbol{k}')}\Delta_{\beta}(\boldsymbol{k}') = \lambda\Delta_{\alpha}(\boldsymbol{k}). \quad (5)$$

Here, $\beta$ labels the FS patch, $v_F^{\beta}(\boldsymbol{k}')$ is the Fermi velocity, and $k'_{\parallel}$ is the tangent component of $\boldsymbol{k}'$. Equation (5) becomes an eigenvalue problem after discretization, with the eigenvector $\Delta_{\alpha}(\boldsymbol{k})$ representing the gap form factor and the eigenvalue $\lambda$ determining corresponding $T_c$ through $T_c \propto e^{-1/\lambda}$. From symmetry analysis (See Supplemental Material, Sec. IV [13]), each solved $\Delta_{\alpha}(\boldsymbol{k})$ is attributed to one of the five irreducible representations of the $D_6$ point group of our model (or $D_3$ point group for real material with spin-SU(2) symmetry), which corresponds to $s, (p_x, p_y), (d_{x^2-y^2}, d_{xy}), f_{x^3-3xy^2}, f'_{y^3-3yx^2}$ wave pairings, respectively. Note that only intraband pairing is considered here.

The filling dependence of the largest pairing eigenvalue for each pairing symmetry in the superconducting regimes is shown in Fig. 4(a) for $J_H = 0.1U$ and in 4(b) for $J_H = 0$, together with the SDW regimes. No obvious difference is found between Figs. 4(a) and 4(b). Figure 4(a) or 4(b) can also be viewed as the phase diagram, which exhibits the following three remarkable features. First, although SDW order induced by FS nesting is present at $\delta_V$ for both $p$ and $n$ fillings, the SC order is only obvious on the $n$ part, because the bands in the $n$ part are flatter, which leads to a higher DOS. Second, the SC order is strong near the SDW regime, as the spin fluctuation there is strong. This feature makes the system look similar to the cuprates. Note that the unphysical divergence of $\lambda$ ($T_c$ will be very high) just bordering the SDW regime is only an artifact of the RPA treatment, which can be eliminated through introducing self-consistent correction to the single-particle Green's function, as done in the fluctuation-exchange approach [50–52]. Third, the SC order on the left side of $\delta_V$ is stronger than that on its right side for the $n$ part. This asymmetry is due to the asymmetry in FS nesting: the FS in Fig. 2(c) (the left side of $\delta_V$) is better nested than that in Fig. 2(a) (the right side of $\delta_V$). All these features are well consistent with experiments.

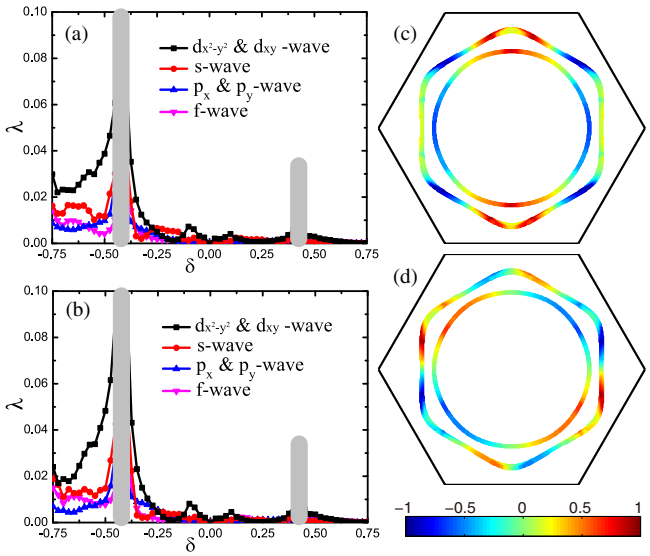


FIG. 4. The doping dependence of the largest eigenvalues $\lambda$ of all pairing symmetries for (a) $J_H = 0.1U$ and (b) $J_H = 0$. Note that the shown eigenvalue for the $f$ wave is the larger one of the two different $f$ symmetries. The vertical bold grey lines indicate the SDW regime. (c) and (d) are the gap functions of $d_{x^2-y^2}$ and $d_{xy}$-wave symmetries at doping $\delta = -0.5$, respectively.

From Fig. 4(a) or 4(b), the leading pairing symmetry near $\delta_V$ relevant to experiment is the degenerate $(d_{x^2-y^2}, d_{xy})$ doublets, with their gap form factors shown in Figs. 4(c) and 4(d). While the gap function of $d_{x^2-y^2}$ depicted in Fig. 4(c) is symmetric about the $x$ and $y$ axes in the reciprocal lattice, that of $d_{xy}$ depicted in Fig. 4(d) is asymmetric about them. This singlet pairing symmetry is driven by the antiferromagnetic spin fluctuations here. Physically, the key factors which determine the formation of $d$ wave SC are the VHS and FS nesting. First, the VHS takes place at the three time-reversal-invariant momenta, which only support singlet pairings [53]. Second, the location of the VHS and the FS nesting vectors on the outer FS here at $\delta_V$ is nearly the same as those of the single-layer graphene at quarter doping [54]. Then, from the renormalization group analysis [54–56], both systems should share the same pairing symmetry, i.e., the degenerate $d$ wave. Therefore, the $d$-wave SC, here, is mainly determined by the features of the FS, and depends little on the details of the repulsive interactions.

The degenerate $(d_{x^2-y^2}, d_{xy})$ doublets will further mix into fully gapped $d_{x^2-y^2} \pm id_{xy}$ $(d + id)$ SC in the ground state to minimize the energy (See Supplemental Material, Sec. V [13]). This chiral pairing state breaks time-reversal symmetry and belongs to class $C$ topological SC [57], characterized by integer topological quantum number $Z$ and, thus, can host topologically protected boundary fermion modes, which appeals to experimental verification.

*Discussion and conclusion.*—Note that there are two FS patches at $\delta_V$ in our model, with only the outer one well nested, as shown in Figs. 2(b) and 2(e). Thus, for weak $U$, the FS-nesting driven SDW order can only gap out the outer FS, leaving the inner pocket untouched. However, as argued in Ref. [1], the interaction strength in the MA-TBG is not weak in comparison to the bandwidth. Therefore, the SDW order might be strong enough to touch and gap out the inner pocket as well, leading to a tiny net gap on that pocket, which might be related to the so-called Mott gap of 0.31 meV detected by experiment [10]. Moreover, this gap caused by the noncoplanar SDW order will easily be closed by Zeeman coupling to an applied external magnetic field [48], driving the metal-insulator transition detected by experiment [1].

The asymmetry on the situation of FS nesting on different doping sides of $\delta_V$ shown in Fig. 2 might also be related to the asymmetry observed in quantum oscillation experiments [1]. As the FS for the side $|\delta| \gtrsim |\delta_V|$ is better nested than that for the other side, it is possible for some range of $U$ that SDW order only emerges on that side, in which case, a small pocket with the area proportional to $|\delta| - |\delta_V|$ only emerges on the side $|\delta| \gtrsim |\delta_V|$, consistent with quantum oscillation experiments [1].

We notice a peak in the DOS near the band bottom, as shown in Fig. 1(c). Careful investigation into the band structure reveals that the peak is caused by band flattening near the bottom. The FS there only includes two small pockets, and no VHS or FS nesting can be found, as shown in the Supplemental Material, Sec. II [13]. In this region, ferromagnetic metal caused by Stoner criteria, instead of SC, might be developed.

In conclusion, our adopted effective $p_{x,y}$-orbital TB model on the emergent honeycomb lattice with the newly constructed hopping integrals well captures the main characteristics of a real system. Remarkably, Lifshitz transitions take place at VH fillings near $\pm\frac{1}{2}$. The VHS and the FS nesting with threefold degenerate nesting vectors drive the system into noncoplanar chiral SDW order, featuring a QAHE. Bordering the chiral SDW phase is $d + id$ chiral topological SC (TSC) driven by short-ranged antiferromagnetic fluctuations. The phase diagram of our model is similar to experiments. Thus, the MA-TBG might provide the first realization of the intriguing $d + id$ chiral TSC proposed previously [54–56,58–62] in graphene-related systems.

We are grateful to the helpful discussions with Fu-Chun Zhang, Yuan-Ming Lu, Qiang-Hua Wang, Yi-Zhuang You, Fan-Qi Yuan, Xian-Xin Wu, Hong Yao, Zheng-Cheng Gu, Yue-Hua Su, Yi Zhou, Tao Li and Yugui Yao. This work is supported by the NSFC (Grants No. 11674025, No. 11774028, No. 11604013, No. 11674151, No. 11334012, No. 11274041), the National Key Research and Development Program of China (Grant No. 2016YFA0300300), Beijing Natural Science Foundation (Grant No. 1174019), and Basic Research Funds of Beijing Institute of Technology (Grant No. 2017CX01018).

*yangfan_blg@bit.edu.cn
†C.-C. L. and L.-D. Z. contributed equally to this work.

[1] Y. Cao, V. Fatemi, S. Fang, K. Watanabe, T. Taniguchi, E. Kaxiras, and P. Jarillo-Herrero, Nature (London) **556**, 43 (2018).
[2] G. E. Volovik, Pis'ma Zh. Eksp. Teor. Fiz. **107**, 537 (2018) [JETP Lett. **107**, 516 (2018)].
[3] B. Roy and V. Juricic, arXiv:1803.11190v1.
[4] H. C. Po, L. Zou, A. Vishwanath, and T. Senthi, Phys. Rev. X **8**, 031089 (2018).
[5] C. Xu and L. Balents, Phys. Rev. Lett. **121**, 087001 (2018).
[6] N. F. Q. Yuan and L. Fu, Phys. Rev. B **98**, 045103 (2018).
[7] G. Baskaran, arXiv:1804.00627.
[8] B. Padhi, C. Setty, and P. W. Phillips, Nano Lett. **18**, 6175 (2018).
[9] J. F. Dodaro, S. A. Kivelson, Y. Schattner, X.-Q. Sun, and C. Wang, Phys. Rev. B **98**, 075154 (2018).
[10] Y. Cao, V. Fatemi, A. Demir, S. Fang, S. L. Tomarken, J. Y. Luo, J. D. Sanchez-Yamagishi, K. Watanabe, T. Taniguchi, E. Kaxiras, R. C. Ashoori, and P. Jarillo-Herrero, Nature (London) **556**, 80 (2018).
[11] See the uppermost two curves in Fig. 4(a) of Ref. [1].
[12] J. C. Slater and G. F. Koster, Phys. Rev. **94**, 1498 (1954).
[13] See Supplemental Material at http://link.aps.org/supplemental/10.1103/PhysRevLett.121.217001 for the derivation of the Slater-Koster formulism from symmetry analysis, more details of our band structure, the multiorbital RPA approach, the $d + id$ superconducting state, and classification of the pairing symmetry, which contains Refs. [14,15].
[14] S. Graser, T. A. Maier, P. J. Hirschfeld, and D. J. Scalapino, New J. Phys. **11**, 025016 (2009).
[15] T. A. Maier, S. Graser, P. J. Hirschfeld, and D. J. Scalapino, Phys. Rev. B **83**, 100515(R) (2011).
[16] N. N. T. Nam and M. Koshino, Phys. Rev. B **96**, 075311 (2017).
[17] P. Moon and M. Koshino, Phys. Rev. B **85**, 195458 (2012).
[18] S. Fang and E. Kaxiras, Phys. Rev. B **93**, 235153 (2016).
[19] J. M. B. L. dos Santos, N. M. R. Peres, and A. H. C. Neto, Phys. Rev. Lett. **99**, 256802 (2007).
[20] J. M. B. L. dos Santos, N. M. R. Peres, and A. H. C. Neto, Phys. Rev. B **86**, 155449 (2012).
[21] S. Shallcross, S. Sharma, and O. A. Pankratov, Phys. Rev. Lett. **101**, 056803 (2008).
[22] R. Bistritzer and A. H. MacDonald, Proc. Natl. Acad. Sci. U.S.A. **108**, 12233 (2011).
[23] R. Bistritzer and A. H. MacDonald, Phys. Rev. B **81**, 245412 (2010).
[24] K. Uchida, S. Furuya, J. I. Iwata, and A. Oshiyama, Phys. Rev. B **90**, 155451 (2014).
[25] E. J. Mele, Phys. Rev. B **84**, 235439 (2011).
[26] E. J. Mele, Phys. Rev. B **81**, 161405R (2010).

[27] A. O. Sboychakov, A. L. Rakhmanov, A. V. Rozhkov, and F. Nori, Phys. Rev. B **92**, 075402 (2015).
[28] E. S. Morell, J. D. Correa, P. Vargas, M. Pacheco, and Z. Barticevic, Phys. Rev. B **82**, 121407R (2010).
[29] G. T. de Laissardiere, D. Mayou, and L. Magaud, Nano Lett. **10**, 804 (2010).
[30] S. Latil, V. Meunier, and L. Henrard, Phys. Rev. B **76**, 201402R (2007).
[31] G. T. de Laissardiere, D. Mayou, and L. Magaud, Phys. Rev. B **86**, 125413 (2012).
[32] J. Gonzalez, Phys. Rev. B **88**, 125434 (2013).
[33] L. A. Gonzalez-Arraga, J. L. Lado, F. Guinea, and P. San-Jose, Phys. Rev. Lett. **119**, 107201 (2017).
[34] Y. Cao, J. Y. Luo, V. Fatemi, S. Fang, J. D. Sanchez-Yamagishi, K. Watanabe, T. Taniguchi, E. Kaxiras, and P. Jarillo-Herrero, Phys. Rev. Lett. **117**, 116804 (2016).
[35] T. Ohta, J. T. Robinson, P. J. Feibelman, A. Bostwick, E. Rotenberg, and T. E. Beechem, Phys. Rev. Lett. **109**, 186807 (2012).
[36] K. Kim, A. DaSilva, S. Huang, B. Fallahazad, S. Larentis, T. Taniguchi, K. Watanabe, B. J. LeRoy, A. H. MacDonald, and E. Tutuc, Proc. Natl. Acad. Sci. U.S.A. **114**, 3364 (2017).
[37] L. Huder, A. Artaud, T. Le Quang, G. T. de Laissardiere, A. G. M. Jansen, G. Lapertot, C. Chapelier, and V. T. Renard, Phys. Rev. Lett. **120**, 156405 (2018).
[38] S.-Y. Li, K.-Q. Liu, L.-J. Yin, W.-X. Wang, W. Yan, X.-Q. Yang, J.-K. Yang, H. Liu, H. Jiang, and L. He, Phys. Rev. B **96**, 155416 (2017).
[39] C. Wu and S. D. Sarma, Phys. Rev. B **77**, 235107 (2008).
[40] C. Wu, Phys. Rev. Lett. **101**, 186807 (2008).
[41] G.-F. Zhang, Y. Li, and C. Wu, Phys. Rev. B **90**, 075114 (2014).
[42] C.-C. Liu, S. Guan, Z. Song, S. A. Yang, J. Yang, and Y. Yao, Phys. Rev. B **90**, 085431 (2014).
[43] F. Yang, C.-C. Liu, Y.-Z. Zhang, Y. Yao, and D.-H. Lee, Phys. Rev. B **91**, 134514 (2015).
[44] K. Kuroki, S. Onari, R. Arita, H. Usui, Y. Tanaka, H. Kontani, and H. Aoki, Phys. Rev. Lett. **101**, 087004 (2008).
[45] X. Wu, F. Yang, C. Le, H. Fan, and J. Hu, Phys. Rev. B **92**, 104511 (2015).
[46] T. Li, Europhys. Lett. **97**, 37001 (2012).
[47] I. Martin and C. D. Batista, Phys. Rev. Lett. **101**, 156402 (2008).
[48] Y. Kato, I. Martin, and C. D. Batista, Phys. Rev. Lett. **105**, 266405 (2010).
[49] S. Jiang, A. Mesaros, and Y. Ran, Phys. Rev. X **4**, 031048 (2014).
[50] T. Takimoto, T. Hotta, and K. Ueda, Phys. Rev. B **69**, 104504 (2004).
[51] K. Yada and H. Kontani, J. Phys. Soc. Jpn. **74**, 2161 (2005).
[52] K. Kubo, Phys. Rev. B **75**, 224509 (2007).
[53] H. Yao and F. Yang, Phys. Rev. B **92**, 035132 (2015).
[54] R. Nandkishore, L. S. Levitov, and A. V. Chubukov, Nat. Phys. **8**, 158 (2012).
[55] W.-S. Wang, Y.-Y. Xiang, Q.-H. Wang, F. Wang, F. Yang, and D.-H. Lee, Phys. Rev. B **85**, 035414 (2012).
[56] R. Nandkishore, R. Thomale, and A. V. Chubukov, Phys. Rev. B **89**, 144501 (2014).
[57] A. P. Schnyder, S. Ryu, A. Furusaki, and A. W. W. Ludwig, Phys. Rev. B **78**, 195125 (2008).
[58] S. Pathak, V. B. Shenoy, and G. Baskaran, Phys. Rev. B **81**, 085431 (2010).
[59] A. M. Black-Schaffer and S. Doniach, Phys. Rev. B **75**, 134512 (2007).
[60] J. Gonzalez, Phys. Rev. B **78**, 205431 (2008).
[61] A. M. Black-Schaffer, Phys. Rev. Lett. **109**, 197001 (2012).
[62] F. Liu, C.-C. Liu, K. Wu, F. Yang, and Y. Yao, Phys. Rev. Lett. **111**, 066804 (2013).